

# Laser Wire Deposition of Thick Ti-6Al-4V Buildups: Heat Transfer Model, Microstructure, and Mechanical Properties Evaluations



N. CHEKIR, Y. TIAN, R. GAUVIN, N. BRODUSCH, J.J. SIXSMITH, and M. BROCHU

This paper investigates the effect of depositing thick laser wire Ti-6Al-4V samples on the developed microstructure and subsequent mechanical properties. First, a thermal model is proposed to get a better understanding on the typical thermal cycles that the material has undergone. It is followed by a discussion on the typical structural features that developed in the as-built condition and following three post deposition heat treatments. A stress relief cycle did not substantially affect the morphology of the developed  $\alpha$  platelets. Annealing and HIP followed by aging favored the coarsening of the post-deposited microstructure. A strengthening in terms of hardness has been observed only after the stress relief heat treatment. Developed static tensile properties were globally below the wrought levels. Stress-relieved specimens developed the higher strengths, whereas the annealed or HIPed samples followed by aging were associated with a better elongation. Charpy impact properties were higher in the annealed or HIPed condition followed by aging when compared with the stress-relieved ones. No anisotropy in the impact toughness properties was observed. The annealed and aged samples and the HIPed and aged samples produced overall very similar results showing that HIP is not required for enhance materials properties of laser wire deposition applications.

<https://doi.org/10.1007/s11661-018-4927-2>

© The Minerals, Metals & Materials Society and ASM International 2018

## I. INTRODUCTION

Ti-6Al-4V is an attractive alloy for the aerospace industry due to its unique combination of strength-to-weight ratio and excellent corrosion resistance.<sup>[1]</sup> However, its high manufacturing cost, in part associated with the generation of substantial material waste during conventional subtractive processing, makes it a niche product to large manufacturing industries such as aerospace, medical, and oil and gas industries.<sup>[2-4]</sup> Additive manufacturing (AM) is then commonly seen as an attractive solution to reduce material waste generation but also lead times.

There are two big AM families for metals: powder bed fusion (PBF) and directed energy deposition (DED) processes. The latter and particularly laser wire deposition (LWD) have had only slight coverage within the commonly used AM processes.<sup>[5-14]</sup> The lower geometrical complexity of the printed parts can account for the

lower interest of LWD as an AM option. LWD, however, often yields to a better structural integrity of the printed components.<sup>[15]</sup> Other advantages of the DED processes include higher deposition rates and the possibility of printing large components.<sup>[16-18]</sup>

Optimizing the materials properties of the printed Ti-6Al-4V components is of great interest to make AM a viable option for the aerospace industry. Researchers are still facing many challenges such as the anisotropy in the developed microstructure and the subsequent anisotropy in tensile properties.<sup>[7,18-21]</sup> Another great challenge is the repeatability of the generated results. As pointed out by Keist and Palmer,<sup>[19]</sup> AM of Ti-6Al-4V is commonly associated with a wide range of properties for which tensile properties can for example either hardly meet minimum cast requirements as set by ASTM F1108 or sometimes exceed the minimum wrought requirements as set by AMS4911. This variability in properties can be associated with the use of different deposition parameters inducing different thermal histories. These deposition parameters include laser power, laser spot size diameter, travel speed, wire feed speed, wire diameter, and deposition strategy among others.<sup>[16,22]</sup> Changing them results in a change of the thermal history of the printed component affecting in turn the developed microstructure and eventually the material properties.<sup>[16,22]</sup>

N. CHEKIR, Y. TIAN, R. GAUVIN, N. BRODUSCH, and M. BROCHU are with the Department of Mining and Materials Engineering, McGill University, Montreal, QC, H3A 0C5, Canada. Contact e-mail: mathieu.brochu@mcgill.ca J.J. SIXSMITH is with Liburdi Automation Inc., Dundas, ON, L9H 7K4, Canada.

Manuscript submitted April 10, 2018.

Article published online September 25, 2018

Many finite element analysis simulations have been proposed in order to predict thermal history, induced distortion, and final phase distribution of the printed components to reduce the variability of the results.<sup>[16,23–28]</sup> However, most of these studies focus on the buildup of thin components. Denlinger *et al.*<sup>[23]</sup> investigated the deposition of larger components with an evolving mesh that reduces the number of elements by merging them and in turn reducing the calculation time. Deposition strategy did not take into account hatch spacing, but rather the activation of a single element on which the heat source would be applied.

The present paper investigates the influence of geometry by printing thick specimens. These specimens include multiple lateral beads within one deposited layer. This is in line with the fact that common printed parts are characterized by cross sections of different dimensions. A heat transfer model with a proposed deposition strategy that takes into account the lateral hatch spacing between two lateral beads was proposed to get a better understanding on the induced thermal history. A look at the typical developed microstructures in the as-built condition but also post deposition heat-treated conditions will be presented and discussed with regard to its thermal history. Subsequent materials properties including hardness, tensile properties, and Charpy impact properties are also presented and discussed with regard to the developed fracture surfaces, microstructures, and textures.

## II. EXPERIMENTAL METHODS

The 3-D heat conduction equation governing the 3-D transient thermal analysis is defined as follows:

$$\rho C_p(T) \frac{dT(r, t)}{dt} = \nabla[k(T)\nabla T(r, t)] + Q(r, t), \quad [1]$$

where  $\rho$  is the material density and assumed to be independent of temperature,  $C_p(T)$  the temperature-dependent specific heat,  $T(r, t)$  the time and space-dependent temperature,  $k(T)$  the temperature-dependent thermal conductivity, and  $Q(r, t)$  is the time and space-dependent heat input.

The part is initially, or in other words when  $t = 0$  seconds, at room temperature  $T_0$ . Newly activated elements are set at the liquidus temperature  $T_L$ .<sup>[16]</sup> Boundary condition at the surface of the specimen is defined as

$$k(T)[\nabla T(r, t) \cdot n]_{\Omega} = h(T(r, t) - T_0)_{\Omega} + \varepsilon\sigma(T(r, t))^4 - T_0^4_{\Omega} - Q_L|_{\Omega_L}, \quad [2]$$

where  $n$  being the external unitary vector normal to the surface,  $h$  is the convective heat transfer coefficient,  $\varepsilon$  is the emissivity,  $\sigma$  is the Stefan–Boltzmann constant,  $Q_L$  is the surface heat flux induced by the laser heat source,  $\Omega$  is the external surface of the part, and  $\Omega_L$  is the surface on which  $Q_L$  is applied.

A typical Gaussian distribution<sup>[16,24–26]</sup> is used to define the laser heat flux  $Q_L$  and is written as follows:

$$Q_L = \frac{2\alpha P}{\pi r_L} e\left(\frac{-2r^2}{r_L^2}\right)_{\Omega_L}, \quad [3]$$

where  $\alpha$  is the absorptivity,  $P$  is the laser power, and  $r_L$  is the laser spot radius.

Evolution of the temperature-dependent thermal properties is shown in Figure 1. The density is assumed constant and equal to  $4430 \text{ kg m}^{-3}$ .<sup>[23,24]</sup> The forced convective heat transfer coefficient is equal to  $55 \text{ W m}^{-2} \text{ K}^{-1}$ ,<sup>[24]</sup> the emissivity is considered fixed at 0.54,<sup>[23,24,27]</sup> and the laser absorptivity has a value of 0.45.<sup>[24,27]</sup>

The finite element analysis software ABAQUS was used to predict the thermal distribution induced by the deposition of new elements. DC3D8 standard eight-node linear heat transfer elements were used. To simplify the model and reduce computation time, a representative substrate of  $25.2 \text{ mm} \times 10 \text{ mm} \times 31.2 \text{ mm}$  was selected as shown in green in Figure 2. Material was deposited on top of one of the two  $25.2 \text{ mm}$  by  $10 \text{ mm}$  surfaces. Width of one bead was approximately  $2 \text{ mm}$ . Deposition of first bead is made on one of the longitudinal sides as seen in blue in Figure 2(a) and the bead's width is associated with two elements. The laser surface is defined on top of the newly activated elements in red in Figure 2(a). Figure 2(b) shows an example where the fifth lateral bead is being deposited. To model the hatch spacing characterized by 50 pct of the bead thickness, the next deposited bead as shown in blue again in Figure 2(b) is obtained by the activation of one new element and the use of another element from the previous bead. The laser surface is at the top of the two elements in red including one newly activated element and one element from the previous deposited bead. All the previously deposited beads are shown in purple in Figure 2(b). Travel speed is characterized by the transient analysis of each activated elements. Time steps of each transient analysis are thus

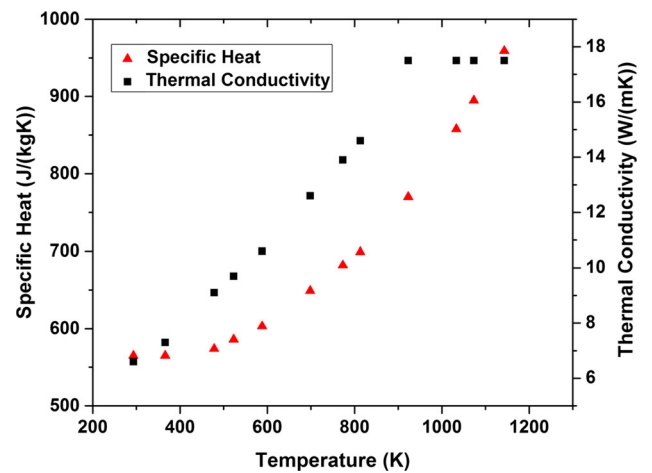


Fig. 1—Temperature-dependent thermal properties.<sup>[23,24,27]</sup>

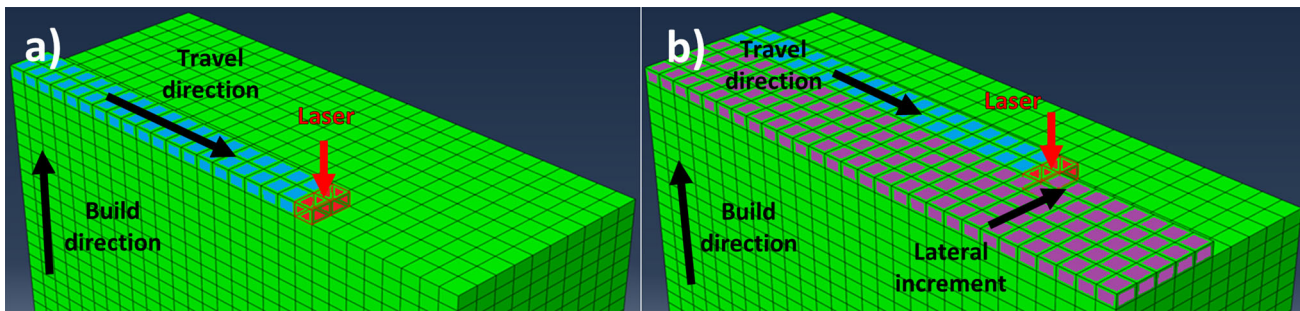


Fig. 2—Activation of new elements in the finite element analysis reproducing the deposition of (a) the first bead of a layer or (b) an intermediate bead within the same layer of thick Ti-6Al-4V specimens using LWD (Color figure online).

Table I. Samples Dimensions

Buildup Type	Substrate			Buildup* Height (mm)
	Height (mm)	Length (mm)	Width (mm)	
Microstructural Analysis	25.4	25.4	11.4	12.7
Tensile	25.4	114.3	11.4	38.1
Charpy				
X	25.4	63.5	11.4	38.1
Z	25.4	38.1	11.4	63.5

\*All builds were produced on one of the two “Length” by “Width” substrate faces for each condition. Buildup height is for reference only and may vary by  $\pm 1.3$  mm.

defined by dividing the bead length with the selected travel speed. Finally, inter-pass waiting time between two deposited beads is set at 25 seconds. This is the time required for the laser head to move from the end of the deposited bead to the initial position of the next deposited bead. The model has in total 14,560 elements and 16,907 nodes. Computation took about 30 hours to complete by using the 64-bit Microsoft Windows 7 Professional operating system associated to a 4 cores Intel® Core™ i7-4770 CPU at 3.40 GHz and with 32.0 GB installed physical memory (RAM). Further details on the simulation data can be found in [Appendix A](#).

AM samples were built using a LAWS 1000 automated deposition system (Liburdi, Hamilton). The robot is controlled by WinLAWS; an in-house software allowing the operator to program axes movements along with defining customized deposition parameters. An IPG Yb:YAG fiber laser (IPG Photonics, Oxford) with a wavelength of  $1070 \pm 10$  nm and reaching up to 1 kW power is used to fuse the material. To prevent excessive oxidation, all deposits are completed in an argon inert environment with oxygen levels below 60 ppm.

Wrought Ti-6Al-4V plates are used as substrates. A Ti-6Al-4V wire spool with extra-low interstitials (oxygen weight percentage being below 0.13 pct) is used to deposit the material. Each deposited layer is made of nine lateral beads with a predefined hatch spacing equivalent to 50 pct of a single bead width. Deposition pattern for one layer was never changed, meaning that travel direction is unchanged and deposition starts always on the same edge and ends always on the same opposite edge. Travel speed is set at  $2.8 \text{ mm s}^{-1}$ . This

speed was selected after a development phase in order to prevent or minimize the risk of developing structural defects such as lack of fusion and pores. A predefined increment of 0.660 mm was set between each deposited layer along the buildup direction. Printed samples are characterized by a width of about 10.16 mm. Length and height were adapted in order to allow evaluation of the developed structure and the extraction of tensile or Charpy impact specimens as summarized in [Table I](#).

Microstructures were evaluated using a Nikon light optical microscope equipped with a Clemex vision system. All samples are mounted in bakelite. These samples were ground up to 1200 SiC grit, followed by polishing with 3 and 1  $\mu\text{m}$  diamond suspension and a finish with 0.05  $\mu\text{m}$  colloidal silica. Grinding and polishing were done using a Buhler Ecomet-3 autopolisher equipped with an Automet-2 head. A Kroll’s Reagent etchant with 91 pct deionized water ( $\text{H}_2\text{O}$ ), 6 pct nitric acid ( $\text{HNO}_3$ ), and 3 pct hydrofluoric acid (HF) was then used on the mounted samples to reveal the structural features using the optical microscope. Phase composition was investigated using a Bruker D8 Discovery X-ray diffractometer with a cobalt source for XRD analysis in the unetched condition. Fractographs were generated using a Hitachi SU-3500 cold field FE-SEM. While texture was analyzed by generating EBSD maps and associated pole figures using a Hitachi SU-8000 cold field FE-SEM along with the EBSD Nordlys II System (Oxford Instrument).

Samples were heat-treated post deposition following two strategies. A stress relief cycle according to AMS2801 standard was performed to reduce the residual stresses while keeping the effect of deposition

**Table II. Selected Heat Treatments**

Heat Treatment	Standard	Cooling Rate	Abbreviation
Stress Relief	AMS2801 (593 °C/2 h)	argon quench	SR
Annealing Followed by Aging	AMS4999 (941 °C/0.25 h)	argon quench	AA
	AMS2801 (482 °C/8 h)	argon quench	
Hot Isostatic Pressure Followed by Aging	AMS4999 (941 °C/138 MPa/2 h)	furnace cooling to aging temperature	HIPA
	AMS2801 (482 °C/8 h)	furnace cooling	

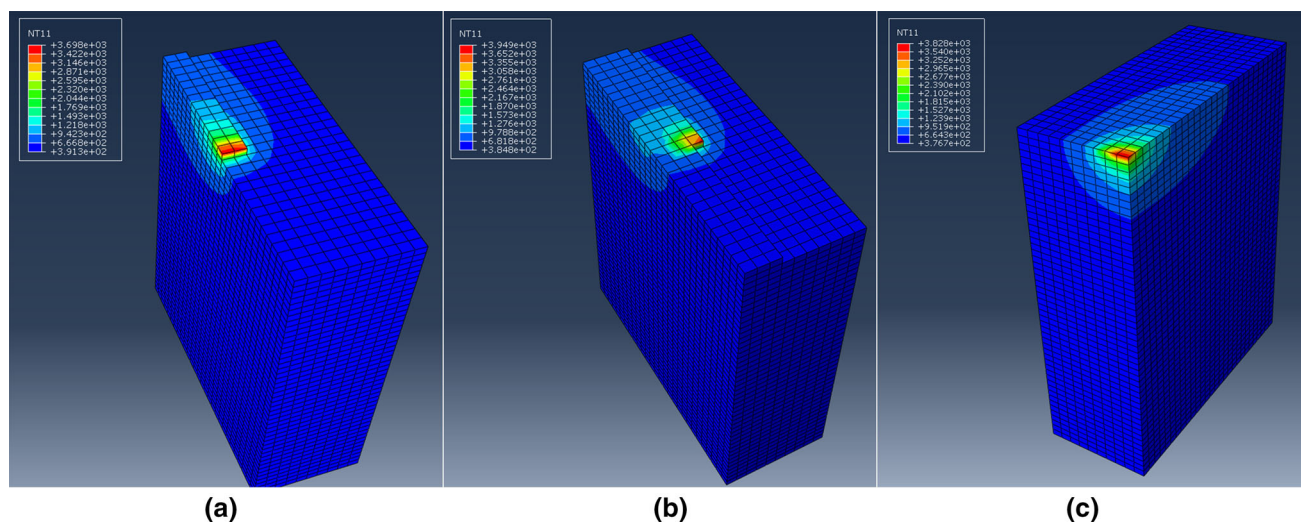


Fig. 3—Temperature distribution while depositing (a) the first bead of a layer, (b) the third lateral bead of a layer, or (c) the last lateral bead of a layer (Color figure online).

parameters on the developed structure. An annealing heat treatment according to AMS2801 or a hot isostatic pressure according to the AMS4999 standard procedure both followed by an aging process according to AMS2801 were also tested in an attempt to remove the effect of deposition parameters and homogenizing the microstructure. Aging soaking temperature following the HIP process was reached by furnace cooling from the hot isostatic pressure temperature. Table II summarizes the heat treatments used in this research and the according abbreviations used for each of them.

The Vickers hardness was measured by means of a Clark Microhardness (CM-100AT) indenter, using a 100 g load. A minimum of 25 measurements was done along the build direction for each of the reported values.

Machined small-size specimens proportional to standard round tension test specimens following the ASTM E8 requirements with a gage diameter of 6.35 mm and a gage length of 25.4 mm were extracted. Three samples per heat-treated condition were tested perpendicular to the build direction and parallel to the travel direction also known as the X direction. Gages of the static tensile samples were positioned within the central region of the buildups. Samples were tested by an independent approved testing facility at room temperature and with a crosshead speed of 2.54 mm min<sup>-1</sup>. Average values of wrought tensile properties produced from five specimens

extracted from the base plate and reproducing the small-size specimens geometry previously described have been used to normalize all the results.

Standard Charpy specimens with a 45 deg V notch were extracted following the ASTM E23 requirements. Six samples per heat-treated condition were tested, three of them along the X direction as defined in the previous section and the other three samples along the build direction also known as the Z direction. Notches regions of all specimens were positioned within the central region of the buildups. Samples were tested at room temperature using a Tinius Olsen Model 74 Universal Impact Tester with a capacity of 358J.

### III. RESULTS AND DISCUSSION

#### A. Thermal Analysis

Figure 3 shows some of the typical isothermal distributions that developed within the deposition process at different stages: during the deposition of the first bead of a layer in Figure 3(a), while depositing the third lateral bead of a layer in Figure 3(b), and at the end of the last deposited bead of a layer in Figure 3(c).

Figure 4 depicts the thermal history of nodes selected from the middle transverse plane to the travel direction. Figures 4(a) through (c) are taken from nodes found at the external edge of the first deposited bead, at the

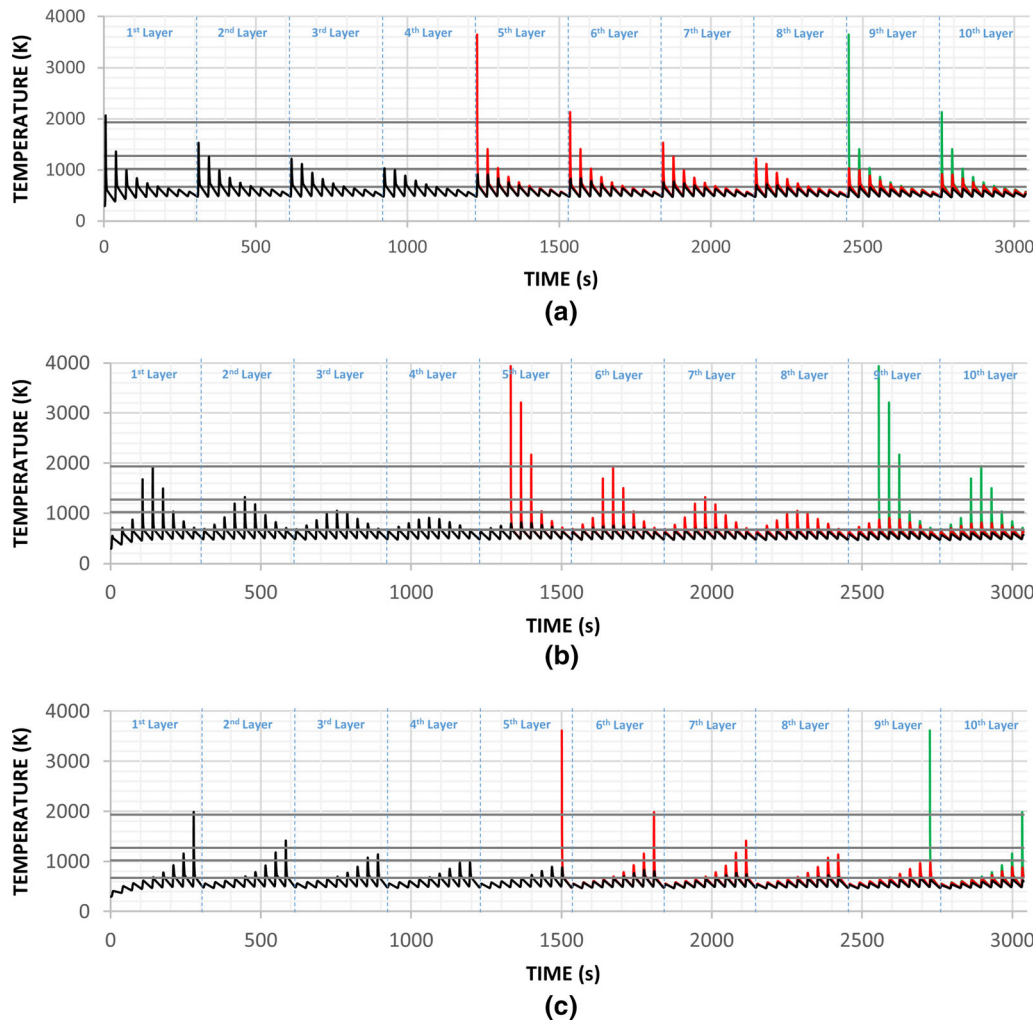


Fig. 4—Time-dependent temperature profiles from the middle transverse plane to the travel direction at (a) the external edge of the first deposited bead, (b) at the center of the deposited layer, and (c) at the external edge of the last deposited bead recorded at the interface between the substrate and deposited material in black, at the top of the fifth layer in red and at the top of the ninth layer in green (Color figure online).

center of the work piece and at the external edge of the last deposited bead, respectively. In each case, one node at the interface between the substrate and the deposited material was selected and represented by the black plots. Another one was selected at the top surface of the fifth deposited layer in red and finally the last node was selected at the top surface of the ninth layer in green. Four important isotherms are shown by horizontal gray lines in the graphs: the melting temperature set at 1660 °C,<sup>[1,29]</sup> the  $\beta$  transus temperature for Ti-6Al-4V set at about 1000 °C,<sup>[1,30]</sup> the temperature at which a visible coarsening of the microstructure occurs and set at about 750 °C,<sup>[31,32]</sup> and finally the martensitic tempering temperature set at about 400 °C.<sup>[26]</sup>

As a general observation, Figure 4 shows that the deposited material did not experience a uniform thermal history with regard to the position of the deposited bead. Figure 4(a) shows that the first deposited bead of a layer goes through initial melting during the deposition and through at least one more partial melting during the deposition of the next layer. Prior  $\beta$  grains will form during the initial stage of the melt pool

solidification and their morphology can be affected in turn by the different experienced melting/solidification cycles. Overall, the deposited bead experiences up to five allotropic transformations. Temperatures exceeding the  $\beta$  transus temperature can also be favorable for a rearrangement of the prior  $\beta$  grains morphology. After the last allotropic transformation,  $\alpha$  platelets are coarsened by the next deposited bead and by the deposition of the two initial beads of the next layer. Tempering of the martensitic microstructure occurs over the next five deposited layers after the occurrence of the last allotropic transformation.

It is interesting to see that a deposited bead at the middle of the buildup in Figure 4(b) can go through at least three melting/solidification cycles induced by the deposition of the initial bead and then by the deposition of the two next lateral beads. Each time, the change in the thermal gradient distribution would affect the morphology of the developed prior  $\beta$  grains. In this case, the deposited bead would go through about six allotropic transformations. Coarsening of the  $\alpha$  platelets after the last allotropic transformation occurs mainly

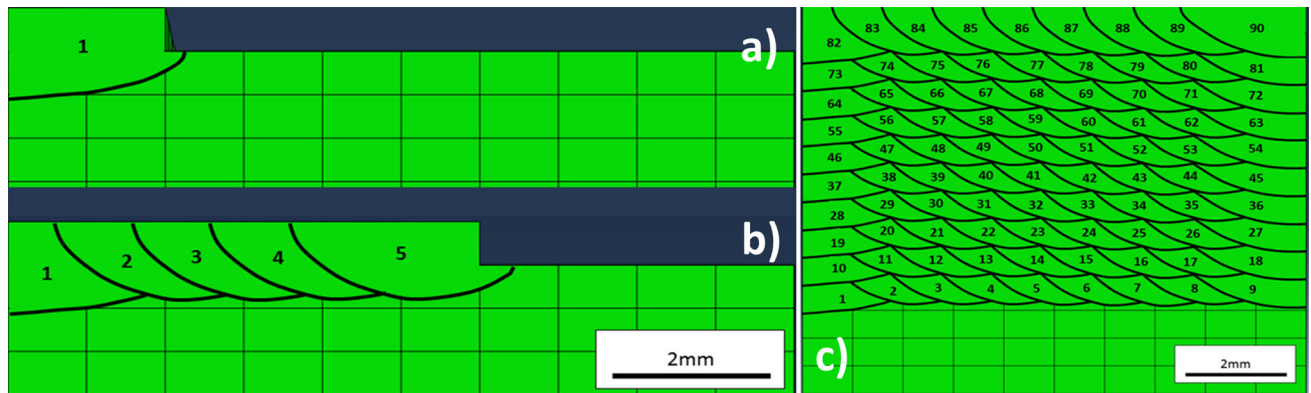


Fig. 5—Computed  $\beta$  transus isothermals in the middle transverse plane to the travel direction following the deposition of (a) the first bead of a layer, (b) the fifth bead of a layer, and (c) the last bead of the tenth layer.

while depositing the next layer and tempering of the martensite over the next four layers. Peak temperatures of all the remaining deposited layers are each time close to the tempering temperature and will also help to transform any martensite that would have formed during the printing process into a more stable combination of  $\alpha$  platelets in a  $\beta$  matrix.

Finally, Figure 4(c) gives information on the thermal history experienced by the last deposited bead of one layer. It shows that one deposited bead hardly goes through another melting/solidification cycle while depositing the last layer. In general, one bead goes through about three allotropic transformations and coarsening of the  $\alpha$  platelets occurs twice after the last allotropic transformation. Tempering of the martensitic microstructure occurs over the next five deposited layers following the last allotropic transformation.

The  $\beta$  transus temperature is as briefly pointed out previously as critical parameter. The  $\beta$  transus isothermals can show the extent of  $\beta$  to martensite  $\alpha'$  or  $\alpha + \beta$  transformations that occurred following the deposition of a single bead. Figure 5 shows the progressive thermally affected areas by the allotropic transformations in the middle transverse plane where all the thermal cycles from Figure 4 were derived. First, Figure 5(a) shows the extent of the computed allotropic transformation that occurred after the deposition of one single bead. The allotropic transformation occurred not only in the deposited material but also within the work piece (either the substrate, the previously deposited beads or a combination of the two). Deposition of an additional bead will in turn induce an allotropic transformation in the newly deposited material, in the last deposited bead and in the work piece. An overlap between the previously thermally affected areas and the new ones will occur and is partially described in Figure 5(b) following the deposition of the fifth lateral bead or globally in Figure 5(c) following the deposition of the ten layers. This amount of overlapping between all the heat affected zones will promote diffusion-controlled solid-state transformations and coarsening of the microstructure upon cooling to room temperature.

## B. Macrostructure

Figure 6 shows the main macroscopic features that developed in the as-built condition and post deposition heat-treated conditions. Samples in this section were very similar in size to the developed thermal model. All macrographs were extracted in a plane containing the buildup direction and that is transverse to the travel direction. These macrographs show that most of the prior  $\beta$  grains exhibit a complex configuration: mostly columnar at the center of the specimens and elongated towards the external side surfaces. Many independent prior  $\beta$  grains of ellipsoidal shape or non-uniform columnar morphology have also been observed scattered all over the buildups as shown by the red arrows. Prior  $\beta$  grains are the first grains that form during the solidification of the melt pool. They are characterized by an epitaxial growth that follows the direction of the steepest thermal gradient.<sup>[9–11]</sup> As seen in the previous section, multiple melting/solidification cycles have probably been experienced by the deposited beads especially within the vicinity of the center of the workpiece. The associated complex developed thermal gradients and the changes in solidification direction in each of these cycles are in line with the development of prior  $\beta$  grains with a complex morphology.

Typical widths of the prior  $\beta$  grains are presented in Table III. Large grains were produced with an average size of 2.4 mm in the as-built condition. Heat treatment did not affect size nor morphology of the prior  $\beta$  grains as seen in Figure 6 and Table III. This was to be expected as none of the post deposition heat treatment temperatures exceeded the  $\beta$  transus temperature at which the allotropic transformation occurs and where recrystallization of the prior  $\beta$  grains can occur.<sup>[33]</sup>

The presence of macroscopic bands as the ones in Figure 6(a) is well documented in the as-built condition of printed Ti-6Al-4V components.<sup>[7–10,15,18,21,34,35]</sup> These are commonly associated with the last allotropic transformation that occurred after the deposition of one bead and are a pure visual effect induced by the arrangements of the  $\alpha$  platelets. However, the reported morphology is typically linear and orthogonal to the deposition direction. This

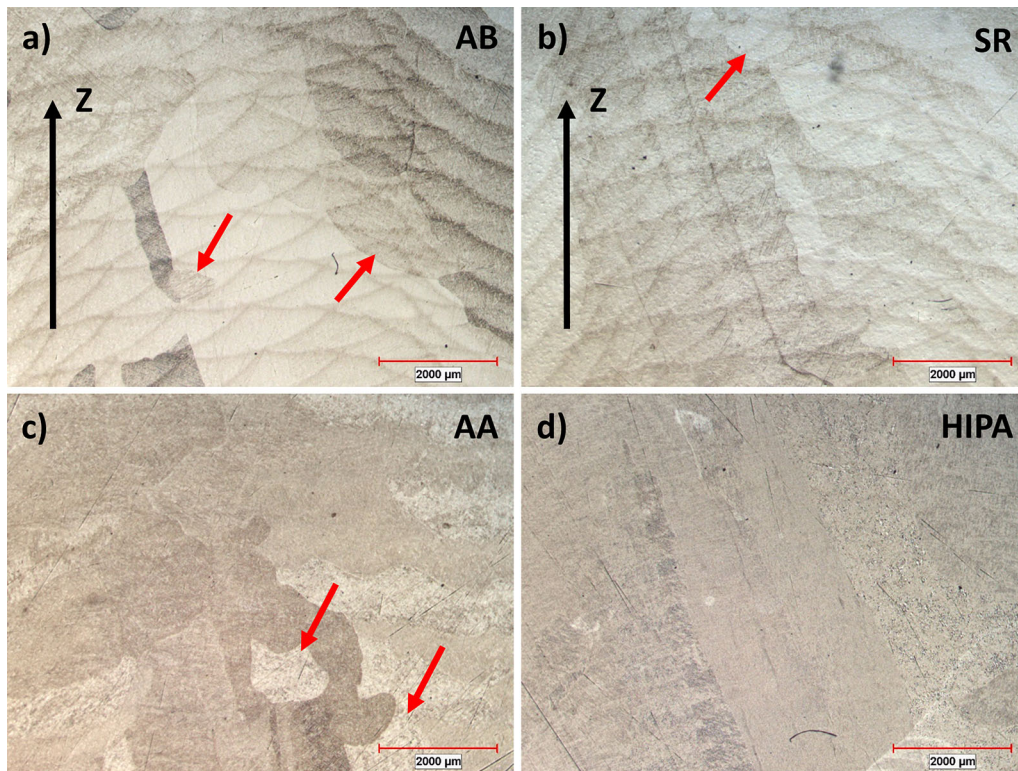


Fig. 6—Macrostructure of the deposited specimens in a transverse plane to the travel direction in (a) the as-built condition, (b) the stress-relieved condition, (c) annealed and aged condition, and (d) HIPed and aged condition (Color figure online).

**Table III. Dimension of Some Key Macro and Microstructural Features**

Heat Treatment	Prior $\beta$ Grain Width (mm)	$\alpha$ Platelets Thickness ( $\mu\text{m}$ )	Globular $\alpha$ Diameter ( $\mu\text{m}$ )
As-built	$2.4 \pm 0.9$	—	—
SR	$2.6 \pm 1.6$	$0.8 \pm 0.5$	$4.8 \pm 1.2$
AA	$2.8 \pm 1.8$	$2.3 \pm 0.5$	$7.7 \pm 2.5$
HIPA	$2.6 \pm 1.3$	$3.4 \pm 0.9$	$11.0 \pm 3.3$

observation is typical of single bead layer buildups.<sup>[15]</sup> The more curved morphology of the present bands attest the more complex thermal history induced by the deposition of multiple lateral beads within one layer. Brandl *et al.*<sup>[10]</sup> presented a similar observation with the deposition of thick Ti-6Al-4V including seven lateral beads per layer. A stress relief heat treatment did not affect the configuration of these bands as shown in Figure 6(b). This was expected as a stress relief cycle does not affect the arrangement of the  $\alpha$  platelets.<sup>[7,10,15]</sup> Moreover, computed  $\beta$  transus isothermals in Figure 5(c) match the experimental observations of the bands morphology. Finally, homogenization of the microstructure through the growth and coarsening of the  $\alpha$  platelets removed the presence of the bands as seen in Figures 6(c) and (d). This is a typical observation made in the previous studies for thin buildups.<sup>[36]</sup>

### C. Microstructure

Microstructures that developed in the as-built condition and post deposition heat treatments are shown in Figure 7. Figure 7(a) shows the typical microstructure

that developed in the as-built condition. The microstructure observed on the left half of the micrograph is usually associated with the morphology of martensitic structures. However, due to the complex thermal history a single bead experienced and the multiple tempering processes as seen in the thermal model, an  $\alpha + \beta$  basket weave type of microstructure with  $\alpha$  platelets in a  $\beta$  matrix is to be expected. This was confirmed with the XRD analysis in Figure 8(a) where a clear  $\beta$  peak appears. The long needle-like structures that appear at the left of the micrograph are associated with long  $\alpha$  platelets within the prior  $\beta$  grain. A stress relief did not drastically change the morphology of the developed microstructure as shown in Figure 7(b). Thicknesses of the  $\alpha$  platelets were measured at  $0.8 \pm 0.5 \mu\text{m}$  as reported in Table III and comparable to the reported thicknesses using this AM process.<sup>[8]</sup> In addition, some globular  $\alpha$  grain were observed with an aspect ratio closer to one. These were about  $4.8 \pm 1.2 \mu\text{m}$  in size. These globular  $\alpha$  grains attest of the slow cooling rates experienced post deposition by one bead allowing diffusional processes to take place. Globular  $\alpha$  grains

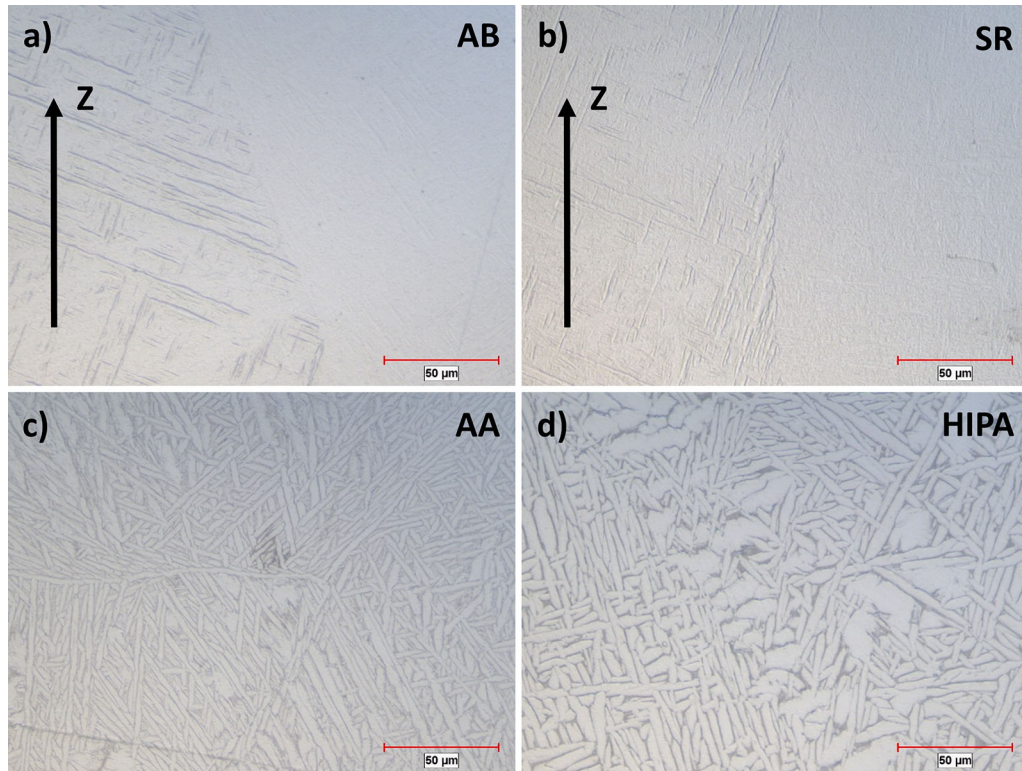


Fig. 7—Microstructures of the deposited specimens in a transverse plane to the travel direction in (a) the as-built condition, (b) the stress-relieved condition, (c) annealed and aged condition, and (d) HIPed and aged condition.

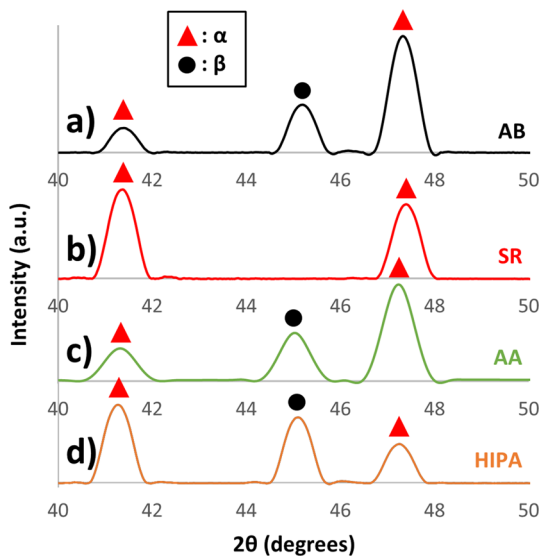


Fig. 8—XRD patterns in (a) the as-built condition, (b) the stress-relieved condition, (c) annealed and aged condition, and (d) HIPed and aged condition.

can then form through the Ostwald ripening and termination migration mechanisms.<sup>[37–39]</sup> The absence of a clear  $\beta$  peak in Figure 8(b) suggests though that most of the  $\beta$  phase transformed into martensite. This can be associated with the soaking temperature being above the martensitic start temperature set at 575 °C<sup>[40]</sup>

and the faster cooling rate induced by argon quenching after the heat treatment cycle transforming most of the  $\beta$  phase into the  $\alpha'$  martensitic phase. A clear coarsening of the microstructure was observed following an annealing or HIP process as seen in Figures 7(c) and (d). This was expected due to the higher soaking temperature that the specimens underwent being closer to the  $\beta$  transus temperature. Long  $\alpha$  grain boundaries have also been observed along with either colonies of  $\alpha$  platelets or needle-like  $\alpha$  platelets with basket weave arrangements in between. Larger platelets and globular grains have been observed in the HIP and aged samples as reported in Table III. This is probably associated with the longer HIP soaking time and slower cooling rate characterizing the transition from the HIP temperature to the aging temperature as pointed out in Table II. No martensite was expected following any of the aging processes as the aging soaking temperature was below the martensitic start temperature for the annealed samples and furnace cooling was performed for the HIPed samples. This was confirmed through XRD analysis in Figures 8(c) and (d) with the presence of a clear  $\beta$  peak in both cases.

#### D. Hardness Evaluation

Hardness results for all the conditions have been summarized in Table IV. Very similar trends as for the single bead buildups have been encountered and are summarized in the following paragraphs.<sup>[15,36]</sup>

Among the main features affecting the Vickers hardness are the material's dislocation density, the solid solution strengthening, grain boundary strengthening, and precipitation strengthening.<sup>[10,12,36]</sup>

The Vickers hardness that developed in the as-built condition is very similar to the observations made in the companion paper for thin buildups at slow travel speed and associated with slower cooling rates.<sup>[15]</sup> Hardness evolution in the as-built condition would mainly be affected by solid solution strengthening due to the presence of some oxygen atoms in the surrounding atmosphere and due to the chemical composition of each phase but also by grain boundary strengthening mainly induced by the morphology of the  $\alpha$  platelets. No precipitation strengthening is to be expected in this process.<sup>[10,15,36]</sup> The impact of dislocation density would be minimized as no martensitic phase is expected in this condition and confirmed by the presence of the  $\beta$  peak in Figure 8.

A stress-relief heat treatment is associated with a strengthening of the deposited material. This was also observed in the previous study of thin buildups.<sup>[15]</sup> However, furnace cooling was used following the thermal cycle as opposed to argon quench in this study. As no drastic change in the  $\alpha$  platelets was observed and no precipitation strengthening was to be expected, the change in hardness can be associated with mechanisms involving dislocation density strengthening and solid solution strengthening. The lack of a  $\beta$  peak in the XRD examination in the previous section suggests the majority of the  $\beta$  phase experienced a martensitic transformation. Even though crystal structure of martensitic phase in titanium is very close to the crystal structure of the  $\alpha$  phase,<sup>[30]</sup> a strengthening mechanism is still expected which would be in agreement with the two remaining strengthening mechanisms.

Finally, an annealing or HIP heat treatment followed by aging were both characterized by a Vickers hardness equivalent to the one developed in the as-built condition. This can be explained by the presence of two competitive phenomena: a softening of the material through the  $\alpha$  platelets coarsening and development of globular  $\alpha$  grains and a strengthening of the material through solid solution strengthening.<sup>[6,8,10,36]</sup>

**Table IV. Hardness Measurements**

Heat Treatment	Hardness (HV)
As-built	313 ± 8
SR	353 ± 8
AA	294 ± 11
HIPA	309 ± 8

## E. Tensile Properties

Tensile properties deriving from the typical developed microstructures presented in Section III-C are reported in Table V. As explained in Section II, tensile properties were normalized with typical wrought properties extracted from sample with similar geometries.

Highest strengths were produced in the stress-relieved condition. However, these were associated with a lower elongation. These observations can be associated with the finer microstructure that developed post deposition and to the presence of martensite that formed post deposition heat treatment.

Annealing and HIP followed by aging produced fairly similar results. They were both characterized by a decrease in strength and an increase in elongation when compared to the stress-relieved samples and associated with the coarsening of the  $\alpha$  platelets. These results show that no HIP heat treatment is required in LWD of thick samples as no major improvement of the properties is noticed.

Generated static tensile results were then compared to the typical results generated using three different DED processes in the literature known as LWD,<sup>[5,6,8]</sup> laser powder deposition (LPD)<sup>[17,21,33,41–44]</sup> and sheet metal deposition (SMD)<sup>[6,45]</sup> as shown in Figure 9. In terms of strengths, the generated stress-relieved results compare well with the as-built LWD results. A stress relief post deposition heat treatment has been reported to either increase strength<sup>[5,6]</sup> or to produce equivalent results as in the as-built condition<sup>[8,15]</sup> for LWD samples while a general increase in strength has resulted for SMD and LPD samples.<sup>[6,41,44]</sup> When comparing the generated strengths levels, it is clear that samples produced using the LPD process generated higher strengths above the typical wrought levels when comparing to results generated using LPD or SMD. This can be associated to the lower heat input and reheat properties of the LPD process. A sub- $\beta$  transus post deposition heat treatment substantially decreased the strengths of tested samples in this study. This is in contrast to what have been observed in other studies for LWD, SMD, and LPD samples.<sup>[6,8,17,33,44]</sup> It is, however, comparable to the drop in strengths reported following a super- $\beta$  post deposition heat treatment and associated to the recrystallization of the prior  $\beta$  grains and substantial coarsening of the microstructure.<sup>[5,33]</sup> This is in agreement with the higher heat input and reheat cycles associated with the present LWD and evaluated in Sections III-A, through III-C. A typical decrease in strength is associated with an increase in elongation when evaluating each process individually. A stress relief post deposition

**Table V. Room Temperature Static Tensile Properties**

Heat Treatment	Yield Strength ((MPa MPa <sup>-1</sup> ) * 100)	Ultimate Tensile Strength ((MPa MPa <sup>-1</sup> ) * 100)	Elongation ((Pct Pct <sup>-1</sup> ) * 100)
SR	87.1 < 87.8 < 88.6, 0.7	85.5 < 87.0 < 88.1, 1.4	19.6 < 27.0 < 33.6, 7.0
AA	75.4 < 76.9 < 78.4, 1.5	78.8 < 80.3 < 82.1, 1.7	47.5 < 54.1 < 61.5, 7.0
HIPA	76.1 < 77.4 < 79.1, 1.5	80.7 < 81.4 < 82.1, 0.7	36.4 < 44.7 < 53.1, 8.4

Results are presented as:  $\sigma_{\min} < \bar{\sigma} < \sigma_{\max}$ , SD where  $\sigma_{\min}$  is the lowest value,  $\bar{\sigma}$  the mean value,  $\sigma_{\max}$  the highest value, and SD the standard deviation from the mean value.

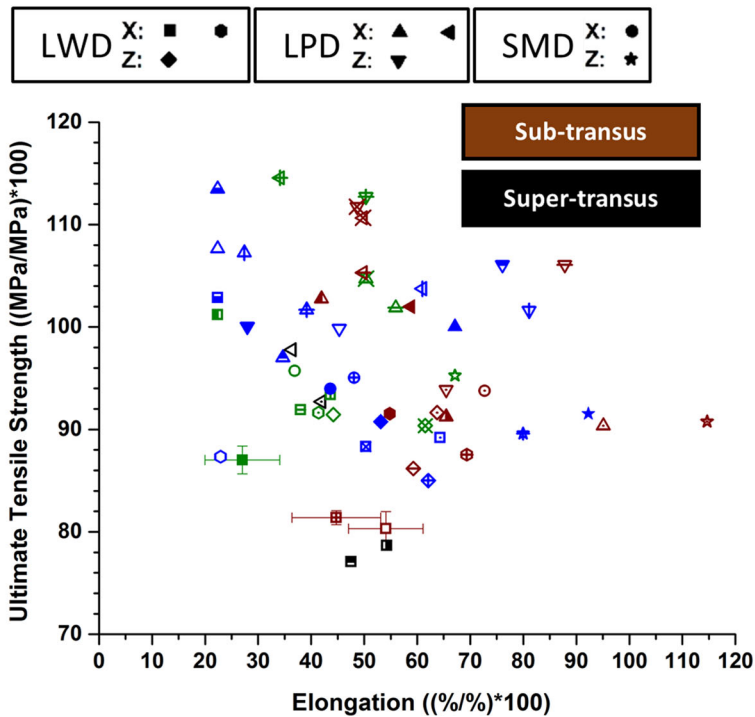
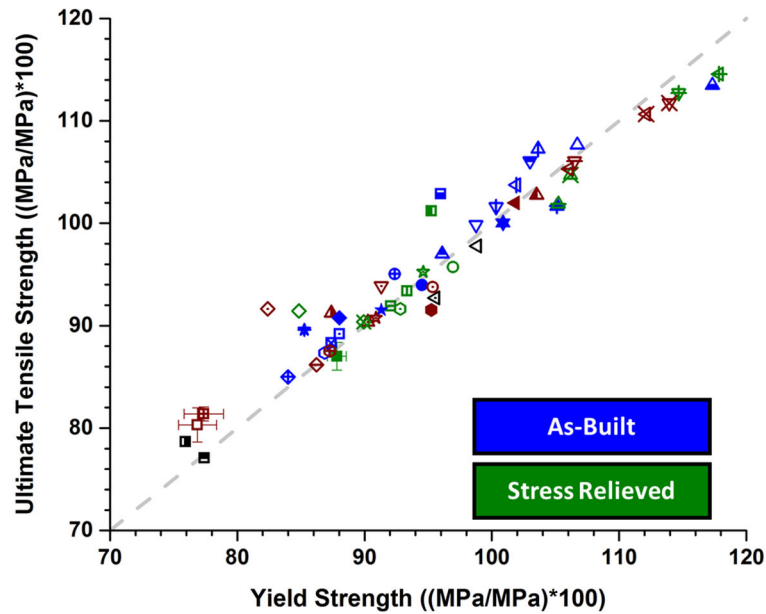
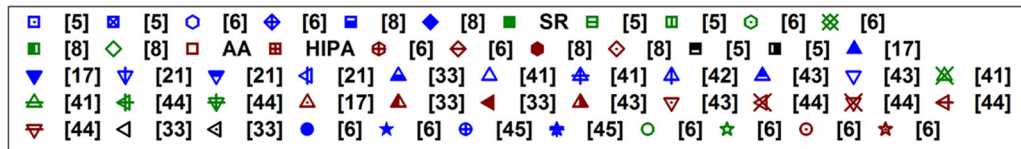


Fig. 9—Investigation of the reported static tensile properties along X or Z at room temperature comparing three different DED processes including LWD, LPD, and SMD in the as-built condition in blue, stress relieved in green, annealed, or HIPed below the  $\beta$  transus temperature with or without aging in brown and annealed or HIPed above the  $\beta$  transus temperature with or without aging in black (Color figure online).

heat treatment affects in different manners the generated elongation depending on the selected process. Both a decrease<sup>[5,8]</sup> or an equivalent<sup>[6]</sup> elongation has been reported for samples processed with LWD. While only a

decrease in elongation has been reported for samples produced with SMD.<sup>[6]</sup> Eventually, an increase in elongation was associated to samples produced with LPD.<sup>[41,44]</sup> Overall, generated elongation following the

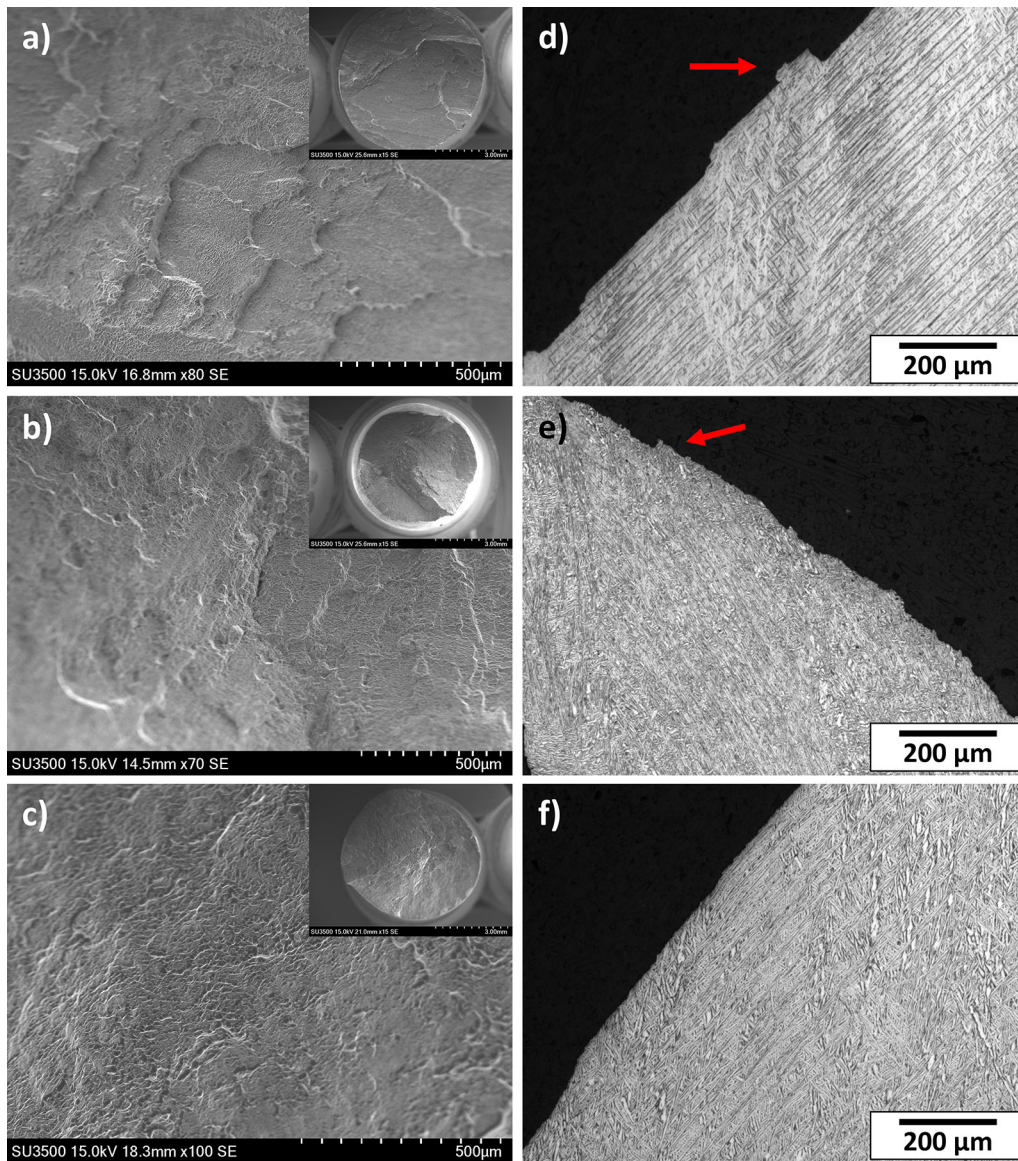


Fig. 10—SEM fractographs of the static tensile specimens in the (a) stress-relieved, (b) annealed and aged, and (c) HIPed and aged conditions along with their respective transverse microstructure at the surface front in (d), (e), and (f) (Color figure online).

stress relief thermal cycle in this study remains within the same range as the elongation reported using the same process. Generated results following a sub- $\beta$  post deposition heat treatment resulted in an increase in elongation and comparable to the increase reported in the literature for the same process.<sup>[6,8]</sup> A similar trend has been reported for SMD<sup>[6]</sup> and LPD<sup>[17,33,44]</sup> samples. This is a common observation and associated to the substantial coarsening of the microstructure.

To get a better understanding of the properties presented in Table V, fracture surfaces were investigated and results are shown in Figure 10. All the fractographs presented the typical dimple morphology characteristic of ductile fracture. Fracture surfaces were either on a 45 deg angle with the loading direction or a more erratic morphology with several fracture planes having different angles as shown for example in the macrograph of

Figure 10(b). The annealed and aged samples presented a more pronounced necking behavior such as shown in Figure 10(b) and measured through the reduction of area at  $37.3 \pm 11$  pct which is in line with the higher elongation shown in Table V. It was followed by the HIPed and aged samples with a reduction of area of  $17.3 \pm 5.1$  pct and the stress-relieved samples with  $13.1 \pm 4.4$  pct. Evidence of terrace-like features was also observed in almost all the specimens. A clear representation of this feature can be seen in Figure 10(a). Microstructural considerations can explain this observation. Indeed, Simonelli *et al.*<sup>[46]</sup> reported a similar feature for PBF processed samples. In this case it was assumed that terraces were associated to the presence of small prior  $\beta$  grains as their aspect ratios were similar. This hypothesis cannot be used in the present study as the developed terrace-like features are

smaller than the developed prior  $\beta$  grains described in Section III–B. These are, however, believed to be driven by changes in the microstructure: presence of the  $\alpha$  platelets within the microstructure would tend to deflect the crack propagation path. Buirette *et al.*<sup>[47]</sup> made this observation in their investigation of the crack propagation in impact specimens with a lamellar microstructure. This seems to be corroborated with the derived fracture micrographs from the same specimens in Figures 10(d) through (f) where steps that match the geometrical properties of the terrace-like features were observed and marked in red. These micrographs also suggest that the crack propagated along preferential directions typically aligned with the needle-like  $\alpha$  platelets.

Texture analysis of the  $\alpha$  phase just below the fracture surface on a plane relatively orthogonal to the fracture surface and containing the tensile testing direction was then produced in the stress-relieved condition. Associated EBSD map and pole figures are shown in Figure 11. The allotropic transformation in titanium alloys follows the Burgers relationship as defined by  $\{0001\}_\alpha || \{110\}_\beta$  and  $\langle 11\bar{2}0 \rangle_\alpha || \langle 1\bar{1}1 \rangle_\beta$ .<sup>[1]</sup> In other words, upon cooling from the metastable  $\beta$  phase above the  $\beta$  transus temperature to the  $\alpha + \beta$  region, one of the six  $\{110\}_\beta$  planes would transform into one  $\{0001\}_\alpha$  plane. The map generated in Figure 11(a) was produced within the same prior  $\beta$  grain. Configuration of the initial bcc crystal structure prior to the solid-state phase transformation was then fairly homogeneous. In turn, only six independent reflections on the basal pole figure would be expected if there is no preferential growth direction for the  $\alpha$  platelets. If multiple prior  $\beta$  grains were to be studied, additional reflections could appear due to the existing misorientation between the different prior  $\beta$  grains as observed by Baufeld *et al.*<sup>[48]</sup> As expected, six main poles are observed in the basal pole figure of Figure 11(c) attesting the more or less random configuration of the  $\alpha$  platelets. However, some of the intensities are stronger than the other ones suggesting that growth of some of the  $\alpha$  platelets still occurred along a preferential direction. Analysis of the other pole figures is more challenging due to the multiple symmetries of the unit hcp crystal structure along with the definition of the Burgers relationship. Indeed, as an example, every hcp unit cell includes three  $\langle 11\bar{2}0 \rangle_\alpha$  independent directions within a single basal plane and related by a rotation of 60 deg. Only one of them would be parallel to one of the two  $\langle 1\bar{1}1 \rangle_\beta$  directions in each of the six  $\{110\}_\beta$  planes of the prior  $\beta$  phase. As a consequence each of the  $\{110\}_\beta$  can produce two different basal planes having the same  $\langle 0001 \rangle_\alpha$  axis but rotated by 70.5 deg around that axis yielding in the end to a rotation of 10.5 deg between two adjacent  $\langle 11\bar{2}0 \rangle_\alpha$  directions extracted from the two possible basal planes.<sup>[34,48]</sup> Each reflection of the basal plane within the basal pole figure could end up having six different  $\langle 11\bar{2}0 \rangle_\alpha$  reflections. Thus, 36 different reflections are to

be expected in the  $\{11\bar{2}0\}_\alpha$  pole figure. As seen before, configuration of the  $\alpha$  platelets is fairly random. As a consequence, intensity on the  $\{11\bar{2}0\}_\alpha$  pole figure in Figure 11(c) is fairly low and confirmed by the scattering of the raw data in Figure 11(b). However, clusters of intensities can be seen in the  $\{11\bar{2}0\}_\alpha$  pole figure within a major reflection that have a triangular shape as shown by the red circle in Figure 11(c). These clusters along with other clusters forming a rhombic pattern but for which intensity was too weak to discern were already reported in the literature and associated with the geometrical considerations discussed previously on the different  $\langle 11\bar{2}0 \rangle_\alpha$  directions that lead to the different poles.<sup>[34,35,48,49]</sup> The lack of intensity and the scattering of the data in the two remaining pole figure are again in line with a more random arrangement of the  $\alpha$  platelets. In the end, combining these results to the other prior  $\beta$  grains within a buildup would induce mostly a random texture within the specimen with slightly localized  $\alpha$  texture. This is supported by Figure 12, for which the pole figures were produced in the same prior  $\beta$  grain as in Figure 10(c) but in a different region and showing a similar distribution of the reflections with a higher intensity for a different reflection in the basal pole figure. Eventually, samples that underwent either an annealing or HIP thermal cycles followed by an aging thermal cycle produced similar results but were not shown in the present study. It is thus not believed that texture would play an important role in the deformation and failure mechanisms but more the local morphology and arrangement of the  $\alpha$  platelets.

#### F. Charpy Impact Testing

Impact properties are important for the aerospace industry in order to assess the material resistance properties in an unpredicted event such as a collision with a foreign body. Few studies in general investigated the impact properties of Ti-6Al-4V<sup>[50–60]</sup> and in particular of printed Ti-6Al-4V.<sup>[59,60]</sup>

Impact properties of PBF processes appear then to be affected by internal structural defects such as pores and lack of fusion.<sup>[59,60]</sup> This is believed to contribute to the anisotropy in the reported results. Impact energy values were also relatively low.

A more thorough investigation on crack propagation during impact testing of Ti-6Al-4V with different microstructures was provided by Buirette *et al.*<sup>[47]</sup> They compared crack propagation in a highly textured bimodal and then a lamellar type of microstructures. It appeared that the combination of texture and microstructure are greatly affecting the impact toughness properties of Ti-6Al-4V. The lamellar microstructure required globally a higher level of energy to fracture in part due to the nature of the  $\alpha$  platelets that prevented the crack from having a linear propagation.

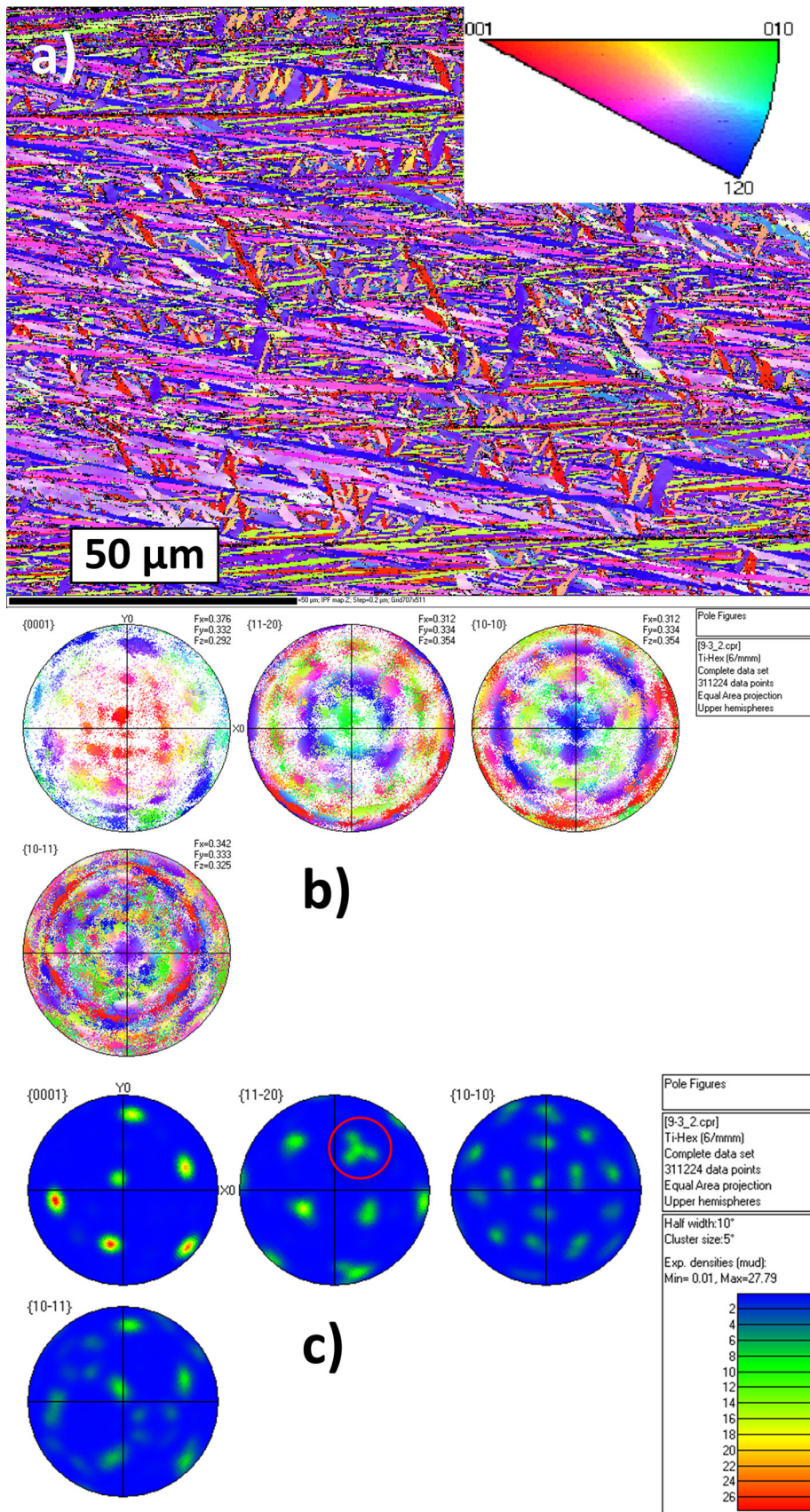


Fig. 11—Texture analysis of the fractured stress-relieved tensile sample. (a) EBSD orientation map below the fracture surface and the associated (b) discrete and (c) contour pole figures (Color figure online).

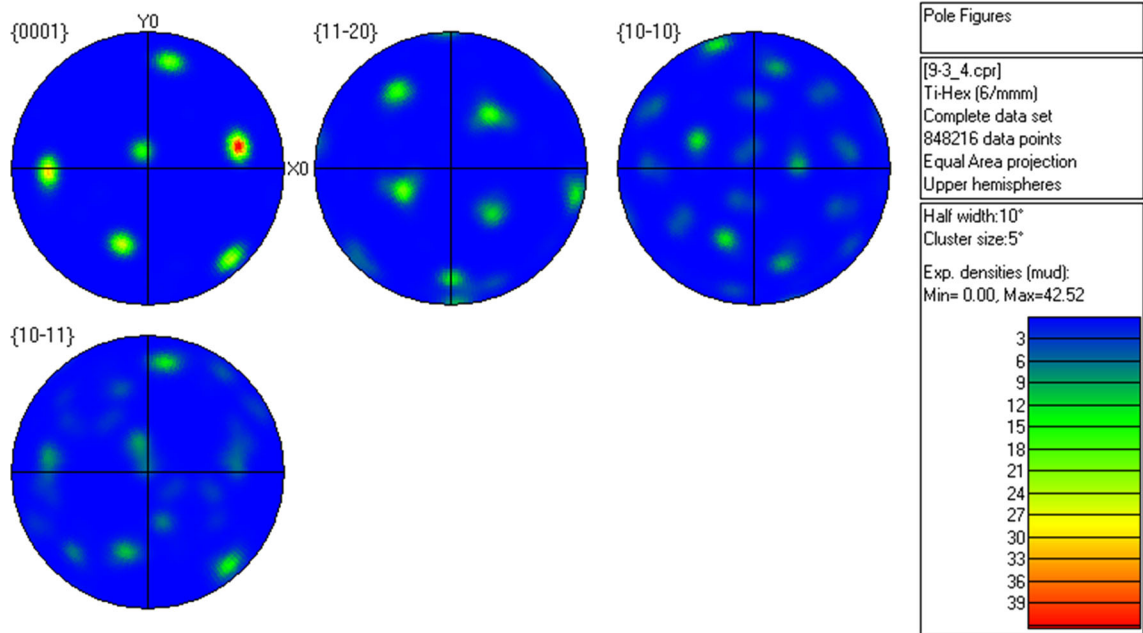


Fig. 12—Contour pole figures extracted from the same prior  $\beta$  grain as in Fig. 11 but in a different region (Color figure online).

**Table VI. Room Temperature Charpy Impact Testing**

Heat Treatment	Direction of Testing	Impact Energy ((J J <sup>-1</sup> ) * 100)
SR	X	216 < 233 < 253, 18
	Z	201 < 222 < 251, 25
AA	X	241 < 281 < 312, 36
	Z	272 < 294 < 312, 20
HIPA	X	241 < 250 < 261, 10
	Z	230 < 234 < 240, 5

Results are presented as  $\sigma_{\min} < \bar{\sigma} < \sigma_{\max}$ , SD where  $\sigma_{\min}$  is the lowest value,  $\bar{\sigma}$  the mean value,  $\sigma_{\max}$  the highest value, and SD the standard deviation from the mean value.

Results generated within this study are provided in Table VI. All results were normalized to typical values generated in the wrought condition.<sup>[1]</sup> Apart from the HIP and aged samples that show a slight anisotropy with regard to the testing direction, most of the results are isotropic in nature. Annealed or HIPed samples followed by aging required a higher energy to rupture with the highest results associated with the annealed and aged specimens. This is in line with the higher elongation produced for both of these conditions. The highest level of energy required for the annealed and aged specimens can be related to the finer  $\alpha$  platelets that were measured in Table III and deflecting at a higher rate the propagation of the crack. The lack in elongation and the likely presence of martensite in the stress-relieved condition can explain in part the lower developed impact energy.

Fractographs were produced in Figures 13 and 14. Fracture surfaces were characterized by the presence of fine dimples typically associated with ductile fracture. All

fracture surfaces were characterized again by the presence of terrace-like features but in higher density than what have been observed for the tensile specimens. These terraces are pointed out by green arrows in Figure 13 and higher magnification fractographs were produced in Figure 14 for some of the selected samples to help in identifying the mechanisms of crack propagation.

Terraces in Figures 14(a) through (c) are believed to be induced by microstructural variations. Micrographs for the same samples generated in Figures 14(d) through (f) tend to confirm the last statement as the step features are of the same order of dimension as the terraces observed in the fractographs. It appears too that fracture is mostly aligned with the developed microstructure and especially with the needle-like  $\alpha$  platelets. It is believed that the lamellar type of structure would oppose more resistance to the propagation of the crack<sup>[47]</sup> and results in the need of more energy to break the samples as seen in Table VI.

Typical texture developed within the stress-relieved sample in the X direction in a plane orthogonal to the notch and to the fracture surface is shown in Figure 15. The EBSD map in Figure 15(a) was again produced within a single prior  $\beta$  grain. Same observations on the different reflections made in the previous section can be adapted to this section as well. It is interesting to see, however, that the main reflections in the basal pole figure but also in the  $\{11\bar{2}0\}_{\alpha}$  pole figure as seen in Figure 15(c) were rotated around the center by the same amount when compared to the pole figures developed in Figure 11(c). This is believed to be associated with the initial configuration of the prior  $\beta$  phase that was most likely different from the one studied in the previous section ending up in the correlated rotation of the new reflections in Figure 15(c). Moreover, samples that

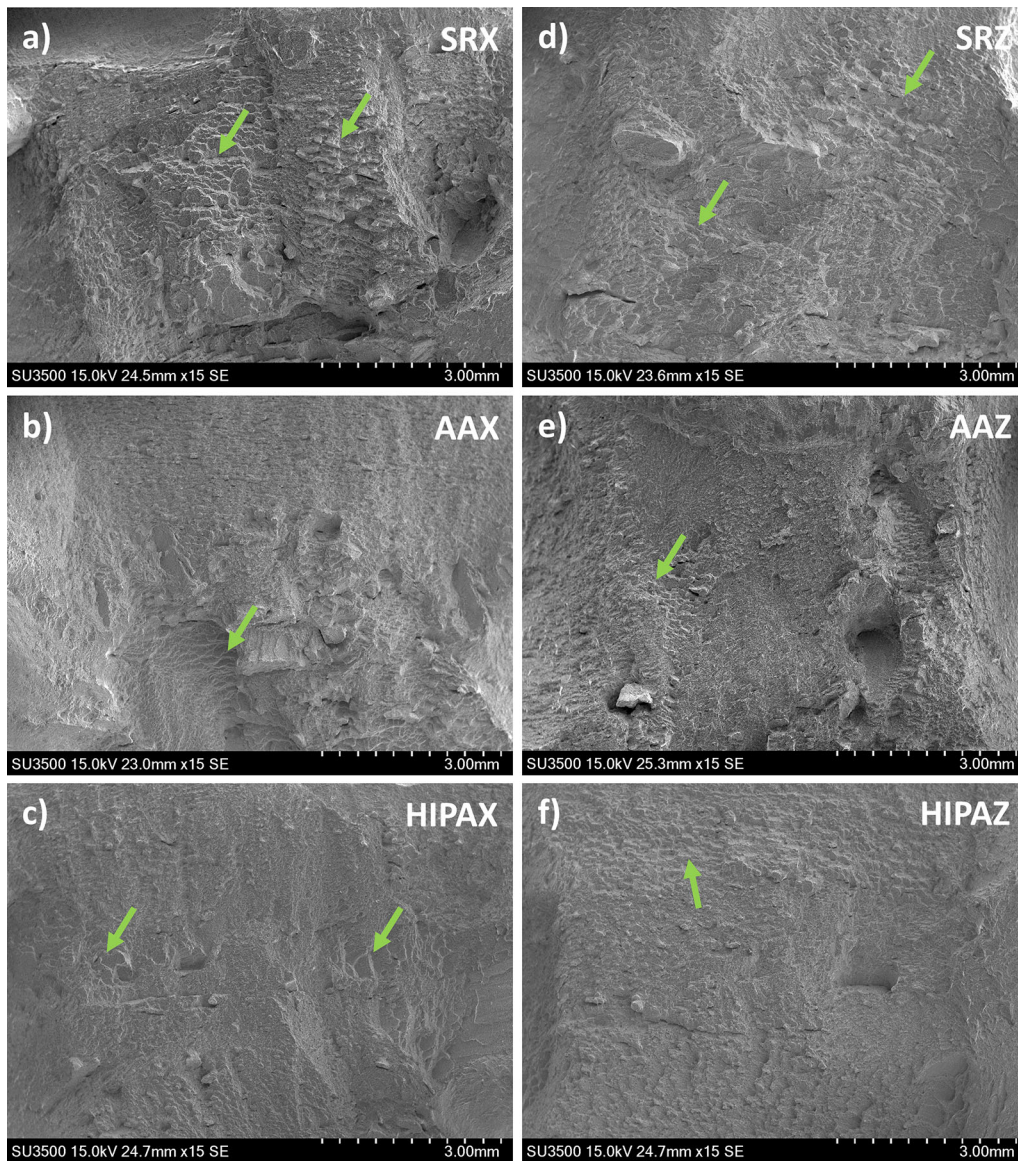


Fig. 13—Fractographs of the Charpy impact samples in the stress-relieved, annealed and aged, and HIPed and aged conditions built along the X direction in (a), (b), and (c), respectively, and in the Z direction for (d), (e), and (f), respectively (Color figure online).

experienced the two other post deposition thermal cycles investigated in this study produced similar results. As a consequence, it is believed again that with the presence of more prior  $\beta$  grains, a random texture mostly developed within the buildups with sometimes some localized stronger  $\alpha$  texture. Crack propagation would then mostly be influenced by the  $\alpha$  platelets morphology and their arrangements as pointed out in the microstructure evaluation in Figure 14.

#### IV. CONCLUSION

The impact of the deposition of thick Ti-6Al-4V specimens on thermal history, structure development, and mechanical properties has been investigated. Conclusions can be drawn as follows:

- A thermal model reproducing the deposition process showed that the printed samples likely went through multiple melting/solidification cycles promoting coarsening of the post-deposited structure and precipitation of the  $\beta$  phase.
- The multiple melting/solidification cycles along with the computed distribution of the  $\beta$  transus temperature isothermal provided more understanding on the complex morphology of the prior  $\beta$  grains and macro bands that formed post deposition.
- A stress relief thermal cycle preserved the morphology of structural features including prior  $\beta$  grains, bands, and  $\alpha$  platelets post deposit arrangements. The high cooling rate to room temperature post heat treatment promoted the development of  $\alpha'$  martensite. This heat treatment was also characterized by a strengthening in terms of hardness of the specimens.

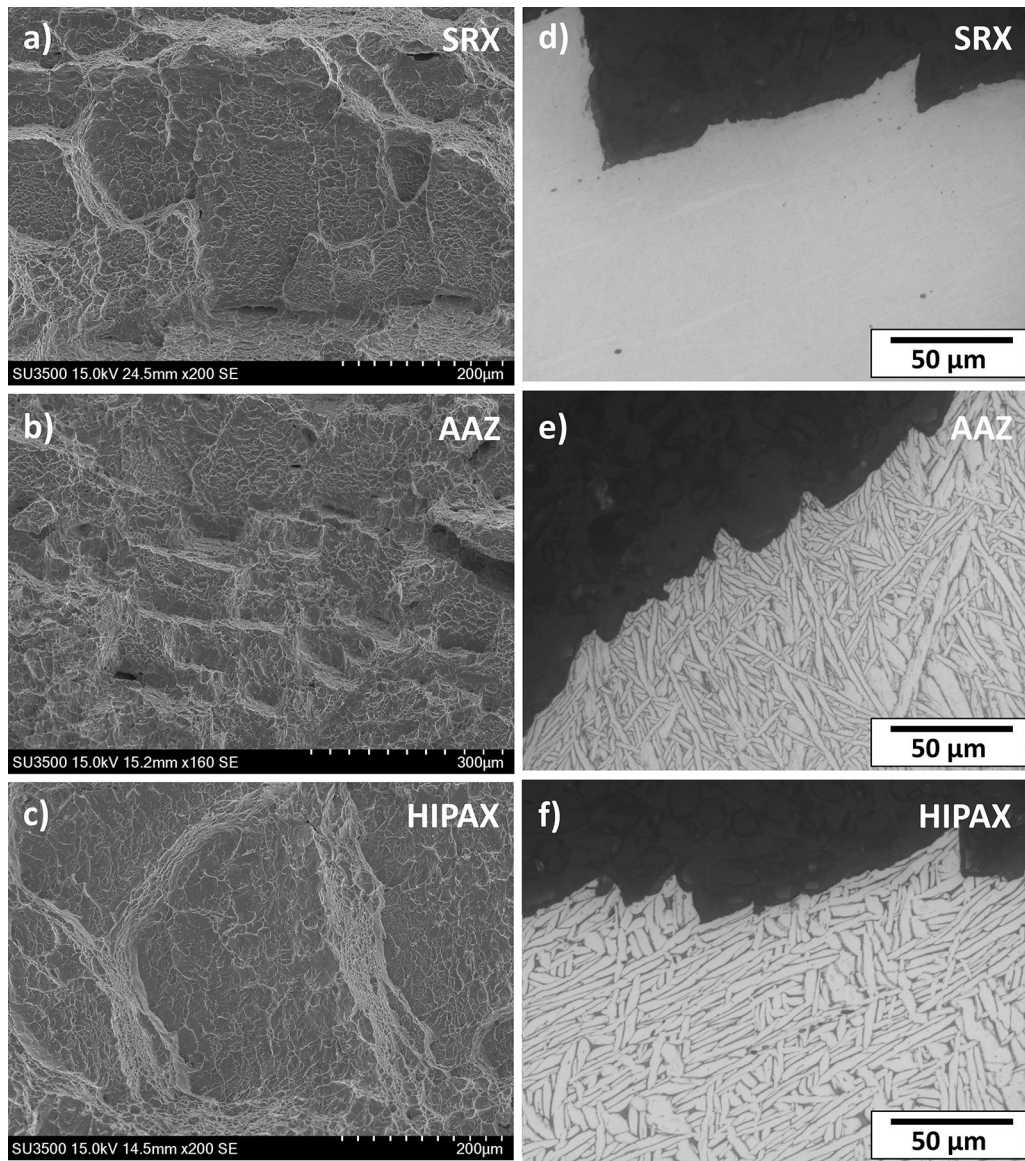


Fig. 14—High-resolution SEM micrographs of the Charpy impacts fracture surfaces and associated optical micrographs for the stress-relieved condition along the  $X$  direction in (a) and (d), for the annealed and aged condition in the  $Z$  direction in (b) and (e), and for the HIPed and aged condition in the  $X$  direction in (c) and (f).

- Annealing or HIP heat treatments followed by aging preserved the morphology of prior  $\beta$  grains but removed the visual bands. An important coarsening of the microstructure has also been reported. No major strengthening in terms of hardness of the heat-treated deposits has been observed when compared to the as-built condition.
- All developed tensile properties were below common wrought values. A higher strength along with a lower elongation was developed in the stress-relieved condition. A HIP and aged heat treatment did not provide any improvement in the static tensile properties nor Charpy impact properties when compared with the annealed and aged specimens.
- Impact properties were mostly independent from the testing direction. The lower elongation of the stress-relieved samples can account for the lower energy values derived in that condition. HIP did not present any additional advantage with regard to the generated results in the annealed and aged condition. The higher energy developed following an annealing or HIP cycles followed by aging were associated with the better elongation and to the morphology and arrangements of the  $\alpha$  platelets.
- Contribution of texture was minimized in front of the morphology of the microstructural features as shown by the presence of terraces on the fracture surfaces and the mostly random orientation of the  $\alpha$  platelets.

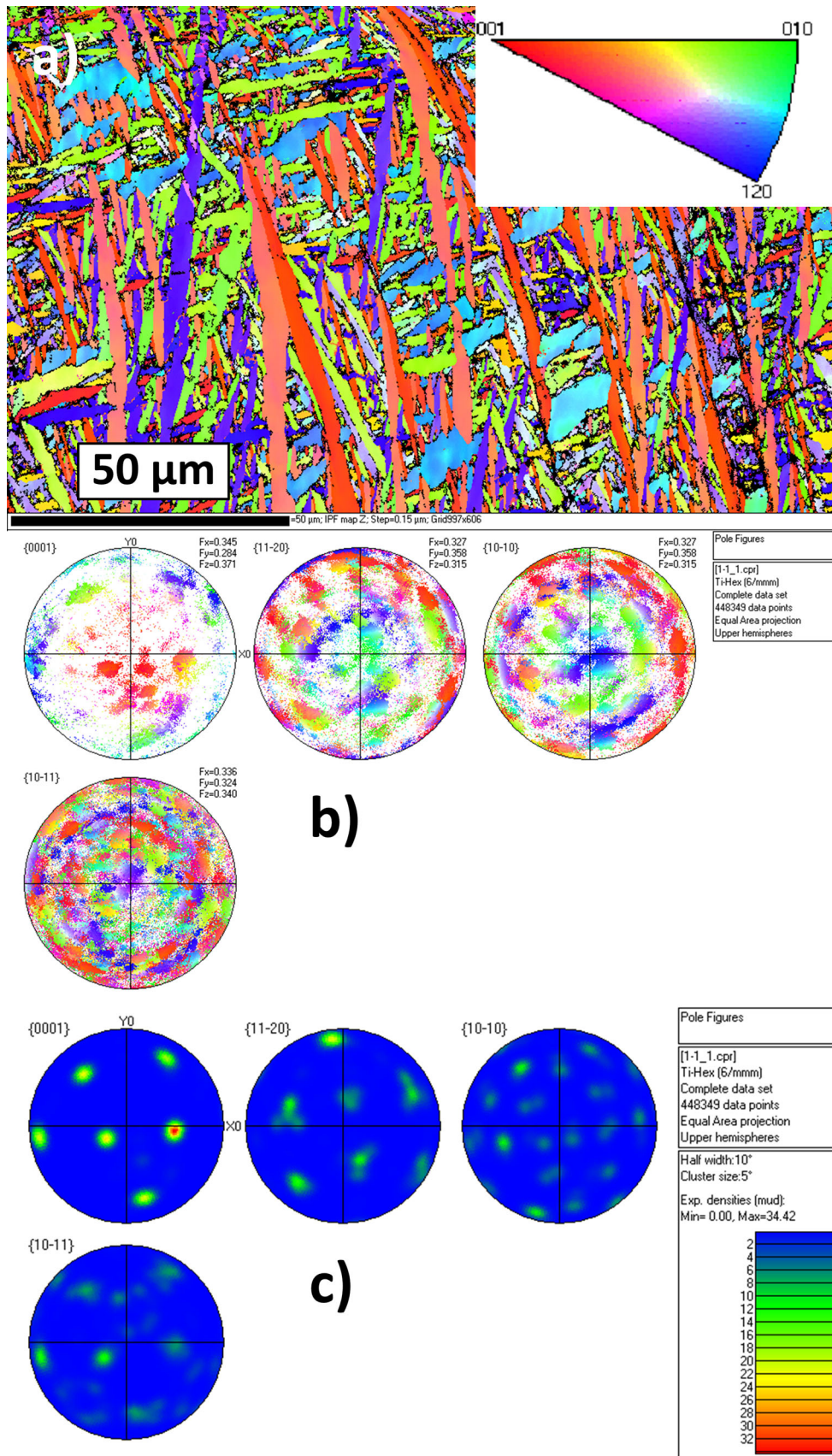


Fig. 15—Texture analysis of the fractured stress-relieved Charpy impact sample. (a) EBSD orientation map below the fracture surface and the associated (b) discrete and (c) contour pole figures (Color figure online).

For further investigation, it will be of interest to understand more in details the effect of deposition parameters including laser power, laser spot size, travel speed, wire cross section, wire feed speed, and travel speed in order to provide optimum process parameters windows to improve experienced thermal history and structural development while maintaining the structural integrity of the Ti-6Al-4V builds. The objective being to reduce reheat of deposited beads while increasing the experienced cooling rates in order to refine the generated microstructure. This will be done in part by improving the simulation work in particular by including a metallurgical simulation through the well-known Johnson–Mehl–Avrami equation and thermomechanical simulation of the builds to eventually validate the simulations to the generated experimental results. Eventually, investigation of the potential anisotropy in static tensile properties will also be of interest.

### ACKNOWLEDGMENTS

The authors would like to thank the Consortium de Recherche et d'Innovation en Aérospatiale au Québec (CRIAQ), Liburdi, Centre de métallurgie du Québec, Bell Helicopter Textron Canada, Bombardier, Edmit, GE, Héroux-Devtek, MDA, and Pratt; and Whitney Canada for their project contribution under the CRIAQ MANU-601/NSERC CRD Grant.

### APPENDIX A: SIMULATION DATA

Simulation data are presented in Table AI.

**Table AI. Parameters Used for a Ti-6Al-4V Multi-Bead Layers LWD Simulation**

Laser Spot Diameter	0.9 mm
Laser Power	765 W
Laser Wavelength	1070 ± 10 nm
Travel Speed	167.6 mm min <sup>-1</sup>
Absorptivity	0.45 <sup>[24, 27]</sup>
Emissivity	0.54 <sup>[23, 24, 27]</sup>
Heat Transfer Coefficient	55 W m <sup>-2</sup> K <sup>-1</sup> <sup>[24]</sup>
Material Density	4430 kg m <sup>-3</sup> <sup>[23, 24]</sup>
Initial Temperature	293.15 K
Ambient Temperature	293.15 K
Liquidus Temperature	1933.15 K
Stefan–Boltzmann Constant	5.67 × 10 <sup>-8</sup> W m <sup>-2</sup> K <sup>-4</sup>
Inter-bead Waiting Time	25 s

### REFERENCES

- G. Lütjering and J.C. Williams: *Titanium*, 2nd ed., Springer, Berlin, 2007, pp. 1–52.
- F.H.S. Froes, M.N. Gungor, and M.A. Imam: *JOM*, 2007, vol. 59, pp. 28–31.
- I. Gibson, D.W. Rosen, and B. Stucker: *Additive Manufacturing Technologies*, Springer, New York, 2015, pp. 1–62.

- C.K. Chua and K.F. Leong: *3D Printing and Additive Manufacturing Principles and Applications*, 4th ed., World Scientific, Singapore, 2014.
- E. Brandl, F. Palm, V. Michailov, B. Viehweger, and C. Leyens: *Mater. Des.*, 2011, vol. 32, pp. 4665–75.
- E. Brandl, B. Baufeld, C. Leyens, and R. Gault: *Phys. Procedia*, 2010, vol. 5, pp. 595–606.
- P. Åkerfeldt, M.-L. Antti, and R. Pederson: *Mater. Sci. Eng. A*, 2016, vol. 674, pp. 428–37.
- B. Baufeld, E. Brandl, and O. Van der Biest: *J. Mater. Process. Technol.*, 2011, vol. 211, pp. 1146–58.
- E. Brandl and D. Greitemeier: *Mater. Lett.*, 2012, vol. 81, pp. 84–87.
- E. Brandl, A. Schoberth, and C. Leyens: *Mater. Sci. Eng. A*, 2012, vol. 532, pp. 295–307.
- E. Brandl, V. Michailov, B. Viehweger, and C. Leyens: *Surf. Coat. Technol.*, 2011, vol. 206, pp. 1120–29.
- E. Brandl, V. Michailov, B. Viehweger, and C. Leyens: *Surf. Coat. Technol.*, 2011, vol. 206, pp. 1130–41.
- S.H. Mok, G. Bi, J. Folkes, and I. Pashby: *Surf. Coat. Technol.*, 2008, vol. 202, pp. 3933–39.
- S.H. Mok, G. Bi, J. Folkes, I. Pashby, and J. Segal: *Surf. Coat. Technol.*, 2008, vol. 202, pp. 4613–19.
- N. Chekir, Y. Tian, R. Gauvin, N. Brodusch, J.J. Sixsmith, and M. Brochu: *Mater. Sci. Eng. A*, 2018, vol. 724, pp. 335–47.
- S.M. Thompson, L. Bian, N. Shamsaei, and A. Yadollahi: *Addit. Manuf.*, 2015, vol. 8, pp. 36–62.
- C. Qiu, G.A. Ravi, C. Dance, A. Ranson, S. Dilworth, and M.M. Attallah: *J. Alloy Compd.*, 2015, vol. 629, pp. 351–61.
- B. Baufeld: *J. Eng. Manuf.*, 2011, vol. 226, pp. 126–36.
- J.S. Keist and T.A. Palmer: *Mater. Des.*, 2016, vol. 106, pp. 482–94.
- S. Wolff, T. Lee, E. Faierson, K. Ehmann, and J. Cao: *J. Manuf. Process.*, 2016, vol. 24, pp. 397–405.
- B.E. Carroll, T.A. Palmer, and A.M. Beese: *Acta Mater.*, 2015, vol. 87, pp. 309–20.
- N. Shamsaei, A. Yadollahi, L. Bian, and S.M. Thompson: *Addit. Manuf.*, 2015, vol. 8, pp. 12–35.
- E.R. Denlinger, J. Irwin, and P. Michaleris: *J. Manuf. Sci. Eng.*, 2014, vol. 136, p. 061007.
- Q. Yang, P. Zhang, L. Cheng, Z. Min, M. Chyu, and A.C. To: *Addit. Manuf.*, 2016, vol. 12, pp. 169–77.
- M. Labudovic, D. Hu, and R. Kovacevic: *J. Mater. Sci.*, 2003, vol. 38, pp. 35–49.
- A. Ahsan: *Convection and Conduction Heat Transfer*, InTech, Shanghai, 2011, pp. 315–40.
- J.C. Heigel, P. Michaleris, and E.W. Reutzel: *Addit. Manuf.*, 2015, vol. 5, pp. 9–19.
- G. Mi, Y. Wei, X. Zhan, C. Gu, and F. Yu: *J. Mater. Process. Technol.*, 2014, vol. 214, pp. 2434–43.
- R. Rai, J.W. Elmer, T.A. Palmer, and T. DebRoy: *J. Phys. D*, 2007, vol. 40, pp. 5753–66.
- M.J. Donachie: *Titanium: A Technical Guide*, 2nd ed., ASM International, Materials Park, OH, 2000, pp. 13–24.
- I. Katzarov, S. Malinov, and W. Sha: *Metall. Mater. Trans. A*, 2002, vol. 33A, pp. 1027–40.
- S.M. Kelly and S.L. Kampe: *Metall. Mater. Trans. A*, 2004, vol. 35A, pp. 1869–79.
- G.P. Dinda, L. Song, and J. Mazumder: *Metall. Mater. Trans. A*, 2008, vol. 39A, pp. 2914–22.
- J.J. Lin, Y.H. Lv, Y.X. Liu, B.S. Xu, Z. Sun, Z.G. Li, and Y.X. Wu: *Mater. Des.*, 2016, vol. 102, pp. 30–40.
- J.J. Lin, Y.H. Lv, Y.X. Liu, Z. Sun, K.B. Wang, Z.G. Li, Y.X. Wu, and B.S. Xu: *J. Mech. Behav. Biomed. Mater.*, 2017, vol. 69, pp. 19–29.
- N. Chekir, Y. Tian, J.J. Sixsmith, and M. Brochu: *Mater. Sci. Eng. A*, 2018, vol. 724, pp. 376–84.
- N. Stefansson, S.L. Semiatin, and D. Eylon: *Metall. Mater. Trans. A*, 2002, vol. 33A, pp. 3527–34.
- N. Stefansson and S.L. Semiatin: *Metall. Mater. Trans. A*, 2003, vol. 34A, pp. 691–98.
- S.L. Semiatin, B.C. Kirby, and G.A. Salishchev: *Metall. Mater. Trans. A*, 2004, vol. 35A, pp. 2809–19.
- T. Ahmed and H.J. Rack: *Mater. Sci. Eng. A*, 1998, vol. 243, pp. 206–11.
- Y. Zhai, H. Galarraga, and D.A. Lados: *Eng. Fail. Anal.*, 2016, vol. 69, pp. 3–14.

42. J. Yu, M. Rombouts, G. Maes, and F. Motmans: *Phys. Procedia*, 2012, vol. 39, pp. 416–24.
43. J. Alcisto, A. Enriquez, H. Garcia, S. Hinkson, T. Steelman, E. Silverman, P. Valdovino, H. Gigerenzer, J. Foyos, J. Ogren, J. Dorey, K. Karg, T. McDonald, and O.S. Es-Said: *J. Mater. Eng. Perform.*, 2011, vol. 20, pp. 203–12.
44. Q. Zhang, J. Chen, Z. Qi, X. Lin, H. Tan, and W. Huang: *Metall. Mater. Trans. A*, 2018, vol. 49A, pp. 3651–62.
45. F. Wang, S. Williams, P. Colegrove, and A.A. Antonysamy: *Metall. Mater. Trans. A*, 2013, vol. 44A, pp. 968–77.
46. M. Simonelli, Y.Y. Tse, and C. Tuck: *Mater. Sci. Eng. A*, 2014, vol. 616, pp. 1–11.
47. C. Buirette, J. Huez, N. Gey, A. Vassel, and E. Andrieu: *Mater. Sci. Eng. A*, 2014, vol. 618, pp. 546–57.
48. B. Baufeld, O. Van der Biest, and S. Dillien: *Metall. Mater. Trans. A*, 2010, vol. 41A, pp. 1917–27.
49. D. Bhattacharyya, G.B. Viswanathan, and H.L. Frase: *Acta Mater.*, 2007, vol. 55, pp. 6765–78.
50. M. Niinomi, T. Kobayashi, and N. Sasaki: *Mater. Sci. Eng.*, 1998, vol. 100, pp. 45–55.
51. J.M. Gómez de Salazar, A. Ureña, and J.G. Carrión: *Scripta Mater.*, 1996, vol. 35, pp. 479–84.
52. M. Balasubramanian, V. Jayabalan, and V. Balasubramanian: *Mater. Lett.*, 2008, vol. 62, pp. 1102–06.
53. D.-G. Lee, S. Lee, and Y. Lee: *Mater. Sci. Eng. A*, 2008, vol. 486, pp. 19–26.
54. T.J. Ma, W.-Y. Li, and S.Y. Yang: *Mater. Des.*, 2009, vol. 30, pp. 2128–32.
55. W. Zhou and K.G. Chew: *Mater. Sci. Eng. A*, 2003, vol. 347, pp. 180–85.
56. K.P. Rao, K. Angamuthu, and P.B. Srinivasan: *J. Mater. Process. Technol.*, 2008, vol. 199, pp. 185–92.
57. L.W. Meyer, L. Krüger, K. Sommer, T. Halle, and M. Hockauf: *Mech. Time Depend. Mater.*, 2008, vol. 12, pp. 237–47.
58. T. Akahori, M. Niinomi, and K.-I. Fukunaga: *Metall. Mater. Trans. A*, 2000, vol. 31A, pp. 1937–48.
59. M.-W. Wu and P.-H. Lai: *Mater. Sci. Eng. A*, 2016, vol. 658, pp. 429–38.
60. E. Yasa, J. Deckers, J.-P. Kruth, M. Rombouts, and J. Luyten: *Virtual Phys. Prototyp.*, 2010, vol. 5, pp. 89–98.